Research Article Vol. 31, No. 2 / 16 Jan 2023 / Optics Express 2523
Optics EXPRESS

Large-scale fabrication of an ultrathin broadband absorber using quasi-random dielectric Mie resonators

XUDONG GUO,[1,2] YU-XUAN REN,[3] LI LI,[1] ZIHUI WANG,[1] SHENZHI WANG,[1] MINGYAN GAO,[1] ZUOBIN WANG,[1,5] AND KENNETH K. Y. WONG[2,4,*]

[1]*International Research Centre for Nano Handling and Manufacturing of China (CNM), Changchun University of Science and Technology, Changchun, 130022, China*
[2]*Department of Electrical and Electronic Engineering, The University of Hong Kong, Pokfulam Road, Hong Kong, SAR 999077, China*
[3]*Institute for Translational Brain Research, Shanghai Medical College, Fudan University, Shanghai, 200032, China*
[4]*Advanced Biomedical Instrumentation Centre, Hong Kong Science Park, Shatin, New Territories, Hong Kong, SAR 999077, China*
[5]*wangz@cust.edu.cn*
[*]*kywong@eee.hku.hk*

Abstract: Ultrathin broadband absorber maintaining a near-uniform low reflectivity over a broadband wavelength is essential for many optical applications, such as light harvesting and nanoscale imaging. Recently, there has been considerable interest in employing arrays of high-index dielectric Mie resonators on surfaces to trap light and reduce the reflectivity. For such Mie-resonant metasurfaces, however, antireflection properties featuring both a flat low reflectance curve and a wide bandwidth are hard to be satisfied simultaneously, and an efficient large-scale nanofabrication technique rarely exists. Here, we present a high-throughput laser interference induced quasi-random patterning (LIIQP) technique to fabricate quasi-random Mie resonators in large scale. Mie resonators with feature sizes down to sub-100 nm have been fabricated using a 1064 nm laser source. Each Mie resonator concentrates light at its shape-dependent resonant frequency, and all such resonators are arranged quasi-randomly to provide both rich (with broadband Fourier components) and strong (with large intensities) Fourier spectra. Specifically, a near-uniform broadband reflectivity over 400-1100 nm spectrum region has been confined below 3% by fabricating a large-scale ultrathin (around 400 nm) absorber. Our concept and high-throughput fabrication technique allows the rapid production of quasi-random dielectric Mie-resonant metasurfaces in a controllable way, which can be used in various promising applications including thin-film solar cells, display, and imaging.

1. Introduction

Reflection is a fundamental optical phenomenon at the interface of two optically homogeneous media [1]. However, antireflection over a broadband wavelength is highly demanded for many photonic and optoelectronic applications, such as imaging [2], display [3] and energy harvesting [4,5]. There have been many mechanisms to confine and control light at the subwavelength scale using high-index micro/nano structures [6,7] to reduce reflection. They are mainly based on the concept of resonances [8]. The incident light is resonantly coupled to different optical modes supported by micro/nano structures, and the resonant modes greatly depend on the incident angles and optical properties of the material at the light wavelengths. For example, Fabry-Perot (FP) resonance is widely adopted by coating specially designed thin films [9] on the surface of an optical component. However, those coatings are sensitive to incident angles, and the coating

#479867 https://doi.org/10.1364/OE.479867
Journal © 2023 Received 2 Nov 2022; revised 28 Nov 2022; accepted 29 Nov 2022; published 10 Jan 2023

Optics EXPRESS

process is highly dedicated. Another novel mechanism involves the concept of surface plasmon resonance supported by plasmonic nanostructures through the coupling of light and surface plasmon polaritons [10,11]. However, intrinsic loss and heat generation are harmful for these optoelectronic devices.

Recently, the Mie resonances [12–15] supported by high-index dielectric nanostructures [16,17] feature with low loss and high efficiency for light trapping and antireflection [18,19]. The scattering and diffraction determine the reflection of the Mie resonator array. In order to achieve a near-uniform low reflectivity over broadband range, the scattering over the Mie resonators has to be distributed to broadband components with large intensities in the Fourier spectra. Usually, the linewidth of the Mie resonant modes is around 100 nm (corresponds to a quality factor of ~10), therefore, it is difficult to achieve broadband antireflection with low reflectivity when identical Mie resonators are aligned together. However, the aggregation of multiple distinct resonant modes with distinct central wavelengths [20] would provide a promising solution. Periodic arrangement combining distinct resonance modes for broadband antireflection can offer strong but limited numbers of reflection dips on the Fourier spectrum [21,22]. Totally random Mie resonators have been proposed [4] to achieve smooth and broadband antireflection, whereas the reflectance is relatively high owing to the rich and weak Fourier components [23]. For application like the energy harvesting, both strong and broadband antireflection is highly demanding. The Mie resonators should be optimized to tailor the strength and number of the components on the Fourier spectra.

Quasi-random nanostructures have been proposed to achieve broadband light trapping, and offer both rich and strong Fourier components [23–26]. They are random and disordered textures in the geometry of each unit cell arranged periodically. In disordered media, light localization occurs when the disorder is above a certain threshold. The scattering of waves due to disorder brings about the Anderson localization of light and electrons [27–29]. However, the reproducible disordered system in the nanoscale is highly desirable to study the light wave propagation except that the quasi-random nanostructures usually require expensive nanofabrication processes [24].

Here, the laser interference induced quasi-random patterning (LIIQP) technique was proposed to fabricate the quasi-random dielectric Mie resonators in large scale. This technique is based on laser interference lithography (LIL) [7,30], which is a high throughput nanofabrication method mostly used to fabricate periodic patterns. We extend LIL's capability to fabricate quasi-random dielectric Mie resonators through controllable dewetting of metallic thin film followed by wet etching. We have corroborated that the Mie resonators with different geometric profiles provide large numbers of distinct resonance modes, and the quasi-random pattern could achieve a near-uniform and low-valued reflectivity over a broadband wavelength range, which is promising to produce high-efficiency thin-film solar cells.

2. Principle of broadband antireflection

2.1. Scattering of Mie resonator

An individual low-loss and high-index dielectric nanostructure, e.g., Si nanopillar (SiNP) supports strong Mie resonances originated from the interaction between simultaneous excitation of electric and magnetic multipoles. Such resonances or modes can be identified from the scattering cross section (SCS) of the dielectric resonator, and the Mie mode can be described by Fano profile [31]. Finite-difference time-domain (FDTD) simulations have been performed to study the scattering properties of individual Mie resonators and the inter-resonator coupling. The material property of the silicon was obtained from Palik's handbook [32]. Figure 1(a) shows the SCS of a SiNP with a diameter of 200 nm and a height of 400 nm in air (red) and on a Si substrate (blue). The resonances are broadened in the presence of substrate, since the light can be efficiently coupled into the substrate, which is manifested by the electric field distribution of the Si resonator in Figs. 1(b) and 1(d). The efficient coupling between the Mie resonator

Optics EXPRESS

and substrate is important for light enhancement at the interface. The backward light scattering is strongly suppressed, whereas the forward light scattering is greatly enhanced. Figure 1(c) shows the forward and backward scattering spectra together with the forward-to-backward ratio of the 200 nm Si resonator. The backward scattering can be almost suppressed when the Kerker condition is satisfied [14]. This can be achieved by tuning the interference of different Mie modes, and the scattering direction and amplitude can thus be controlled.

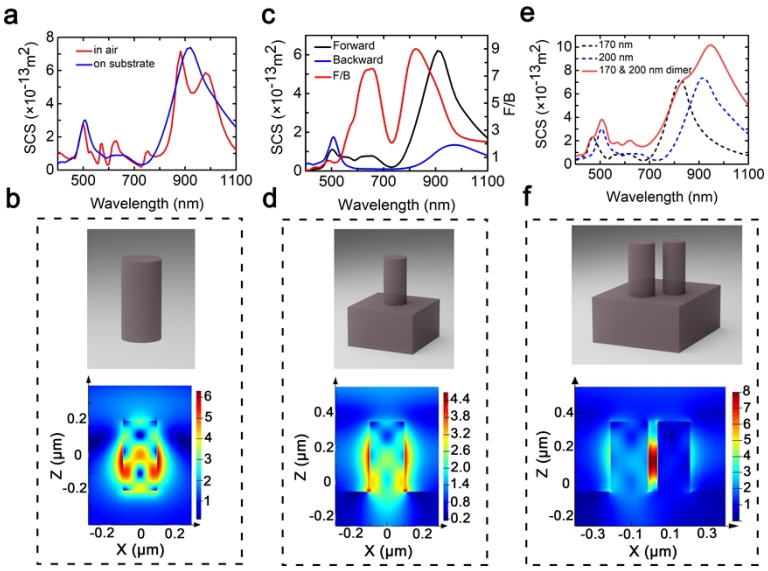

Fig. 1. (a) SCS of a single SiNP with a diameter of 200 nm in air and on a Si substrate. Electric field distributions of a single SiNP with a diameter of 200 nm in air at the wavelength of 882 nm (b) and on the substrate at the wavelength of 921 nm (d). (c) Forward and backward scattering spectra of a single SiNP with a diameter of 200 nm together with the forward-to-backward scattering ratio. (e) SCSs of a single SiNP with the diameters of 170 nm and 200 nm, and a dimer of the two non-identical SiNPs. (f) Electric field distributions of a dimer of SiNPs with the diameters of 170 nm and 200 nm at the wavelength of 949 nm. All individual SiNPs have the same height of 400 nm.

The scattering property of a Mie resonator is closely related to its geometry. For a Si resonator with a diameter of 170 nm, and a height of 400 nm on a Si substrate, the resonance peak takes place at 823 nm, however, a red shift of the resonance peak is observed at 921 nm for a Si resonator with the diameter of 200 nm and the same height. When the two different resonators are combined to form a dimer [33,34], for which the gap between Si resonators is 50 nm, the resonances are broadened, owing to the strong intercoupling of the dimer that covers the overlapped resonance region of the two different Si resonators (Fig. 1(e), 1(f)). Figure 1(f) shows the electric field distribution of the dimer at the resonant wavelength of 949 nm. A near-field electric hotspot in the gap strongly confines the light inside the near-field [35]. Therefore, the resonators with different resonant frequencies should be coupled together to achieve broadband light harvesting.

2.2. *Quasi-random Mie-resonant metasurface*

An individual Mie resonator has narrow scattering spectrum, however, the location of the spectrum peak is associated with the geometry of the resonator. This could be applied to design the metasurface using Mie resonator array to achieve broadband performance. As an example, we tune the aspect ratio of a SiNP, specifically, the height of the SiNP is fixed at 400 nm, and the diameter of the SiNP varies from 50 nm to 300 nm. The resonance peak shifts with respect to

Optics EXPRESS

the diameter of the SiNP as corroborated in the SCS spectrum map (Fig. 2(a)). The scattering efficiency is then evaluated from the normalized SCS (Fig. 2(b)).

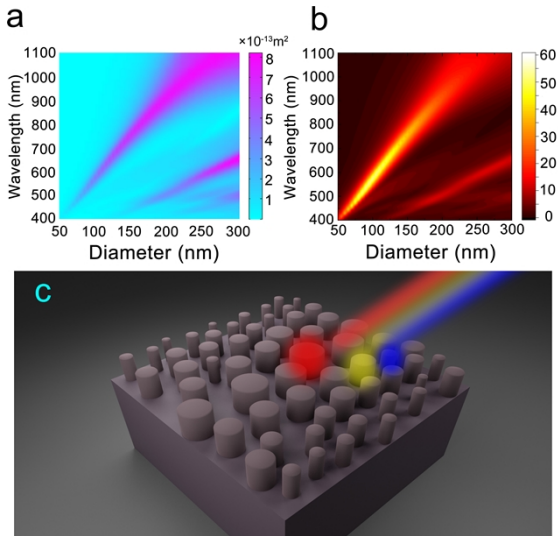

Fig. 2. Scattering cross sections (a) and Mie efficiency (b) of different-sized SiNPs with the same height of 400 nm; and proposed supercell (c) of the quasi-random metasurface.

Metasurfaces composed of periodic Mie resonator array have been proposed to reduce the reflection, however, the reflectivity is considerably low over a narrow spectrum range [22]. Because their shapes and sizes are usually identical, so that multiple resonances cannot be excited across a broadband spectrum. We would arrange the Mie resonators in multiple geometries to achieve broadband antireflective performance. In order to gain a relatively comprehensive insight into the collective Mie scattering or diffraction characteristics of the metasurface, momentum (or reciprocal) space was applied by transforming the scattered light into the Fourier spectrum. For periodic metasurface, strong but limited numbers of Fourier components are excited, which is corroborated by the limited numbers of reflectance dips [23]. Random Si resonators with fixed sizes have been proposed to achieve broadband antireflection [4], which can excite many Fourier components [23]. However, they are too weak to achieve low reflection. Therefore, it would be reasonable to design a dielectric metasurface with Mie resonators of quasi-random sizes and locations. The quasi-random resonators can excite strong and sufficient Fourier components for broadband antireflection. We here designed a supercell [23] with quasi-random nanopillars (Fig. 2(c)). Large Mie resonators are located at the center of the supercell metasurface, which trap (reflect) the longer (shorter) wavelength of the light, whereas, the gradually varied small Mie resonators close to the edge of the supercell are designed to trap (reflect) the shorter (longer) wavelength light.

3. Fabrication process of quasi-random Mie-resonant metasurface

3.1. General fabrication process of LIIQP

Dielectric metasurfaces are usually fabricated by complex lithography facilities, such as electron beam lithography [21], reactive ion etching [24], or focused-ion beam lithography [22]. Though precision is guaranteed, these methods are generally time-consuming, and not suitable for massive production. Other fabrication techniques such as self-assembly methods [36,37], laser direct writing [38], and chemical methods [38] are also widely exploited to fabricate dielectric

Optics EXPRESS

metasurfaces and metamaterials. Among them, chemical methods such as metal-assisted chemical etching (MACE) [39] are promising for high-throughput fabrication of low-reflectivity dielectric surfaces for applications like silicon solar cells, however, accompanied by low precision and limited patterns. Most importantly, the thickness of the fabricated nanostructures is usually at a scale of tens of micrometers to efficiently reduce the surface reflection based on the multiple internal reflection mechanism. However, our proposed principle based on Mie resonators is more promising to fabricate ultrathin silicon solar cell with a thickness of several hundreds of nanometers.

Here, we introduce LIIQP, which is a simple, efficient and high-throughput nanofabrication technique to produce the broadband antireflection metasurface. Single-pulse laser interference lithography (LIL) is firstly applied to control the dewetting process of metal film and fabricate the quasi-random metallic pattern [40]. MACE is further applied to etch the quasi-random metallic pattern into Si substrate and produce the final quasi-random Mie-resonant metasurface [41].

We developed the LIIQP setup to fabricate the metasurface with quasi-random Mie resonators (Figs. 3(a) and 3(b)). A thin Ag layer is firstly deposited on the Si substrate. Next, diffraction-unlimited Ag nanopattern is directly written by LIL after single pulse exposure. LIL allows single-step controllable dewetting of Ag film. The Ag nanopattern functions like a photoresist or template and is further etched into Si substrate by MACE. The Ag film is then removed by HNO_3 to produce the corresponding Si-based Mie-resonant metasurface. Figure 3(c) shows a scanning electron microscope (SEM) image of quasi-random Mie-resonant metasurface fabricated in a $100 \times 150\ \mu m^2$ area. In contrast to traditional single pulse LIL with a feature size limited to half of the illuminating wavelength (532 nm) [42], our approach takes advantage of the controllable dewetting of Ag film by LIL to reduce the feature size down to one-tenth the illuminating wavelength (1064 nm), i.e., 100 nm. Moreover, broadband antireflection is guaranteed by the quasi-random pattern made by LIIQP.

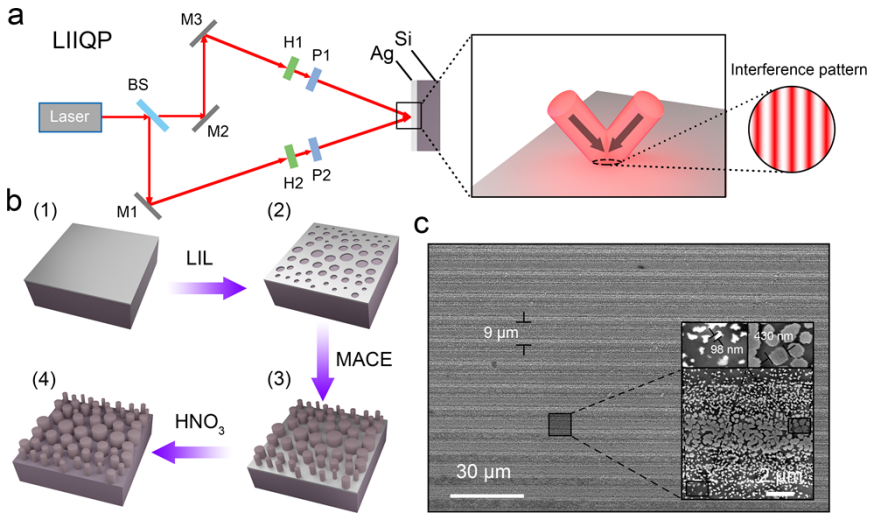

Fig. 3. (a) LIIQP setup, where BS is the beam splitter (1:1), M1, M2 and M3 are the high-reflective mirrors, H1 and H2 are the half wave plates, and P1 and P2 are the polarizers. (b) General fabrication process of quasi-random Mie-resonant metasurfaces. (c) SEM of obtained large-scale quasi-random Mie-resonant metasurface.

In our proposed scheme, the size distribution and height of the Mie resonators can be precisely controlled through the LIIQP process. The patterned area could be efficiently scaled up from mm^2 to cm^2 through overlapping between adjacent interference spots by using high-accuracy

Optics EXPRESS

positioning stages, which is promising for high-throughput, low-cost and mass production. For industrial applications with higher throughput, the fabricated pattern can be used as a stamp to combine with the nanoimprint lithography [38]. The fabricated dielectric metasurface can be extended to more complex quasi-random Mie-resonant metasurfaces for various applications, including thin-film solar cells and nanoscale imaging.

3.2. *Mechanism of single-pulse laser interference controlled dewetting*

The desired quasi-random Mie-resonant metasurface is predefined by metallic template using LIL, and LIL allows the precise control of the dewetting process of thin metallic film. Dewetting of thin metallic film in principle is the mass transport and surface diffusion of the film in order to minimize its surface energy caused by external laser intensity or temperature variation. As shown in Fig. 4(a), Ag nanoholes (AgNHs) are firstly observed at a lower irradiation intensity. The nanoholes further break up into small Ag nanoparticles (AgNPs) with the increase of intensity. Adjacent small AgNPs would aggregate into large ones at higher intensity.

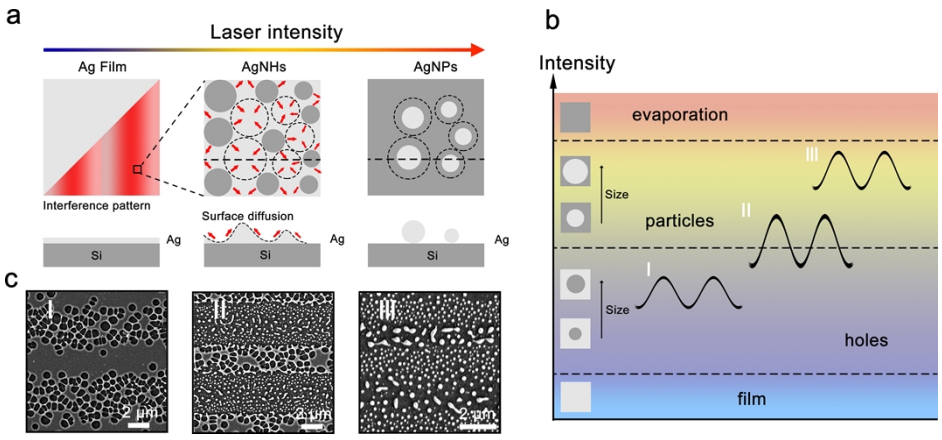

Fig. 4. (a) Mechanism of two-beam laser interference induced dewetting of Ag film with the increase of laser intensity. (b) Different dewetting stages influenced by the laser irradiation intensity. The dashed lines indicate the threshold condition. The intensity difference between the local maximum and minimum of laser interference field can be controlled to fabricate the required configuration of metallic nanostructures. (c) SEM images of quasi-random metallic metasurface under different irradiation conditions.

Since the dewetting of thin metallic film is very sensitive to the laser intensity variation. Therefore, by precisely controlling the intensity or temperature gradient along one interference period, multiscale nanostructures including nanoholes and nanoparticles with feature sizes down to one-tenth the illuminating wavelength can be fabricated (Figs. 4(b) and 4(c)).

4. Experiment

The P-type (100) dielectric silicon wafers were cut into 1 cm by 1 cm as the substrate. The substrates were ultra-sonicated with acetone, ethanol, and deionized water in sequence. Then, the Ag film with 20 nm thickness was deposited on the substrates by an ion-sputtered coater (Quorum Technologies Q150T). The quasi-random Ag nanopattern was subsequently obtained under a single pulse exposure by LIL. The light source was a high-power pulsed Nd: YAG laser with the wavelength of 1064 nm, pulse duration of 7 ns, maximum pulse energy of 2J, and Gaussian beam diameter of 6 mm. The output energy from the laser source can be controlled by altering the laser voltage. The combination of polarizers and half wave plates was used to control the output

Optics EXPRESS

energy of a single beam, which was measured by an energy meter (Coherent LabMax-top, Santa Clara, California). To make sure two laser pulses overlap in time and produce interference pattern at the sample surface, the two optical paths after the beam splitter (Fig. 3(a)) were carefully aligned and adjusted to ensure that they have the same optical path length [30]. Quasi-random Si metasurface was subsequently fabricated by MACE of the corresponding Ag nanopattern in a solution composed of 10% HF and 0.6% H_2O_2 for around 10 minutes. 65% HNO3 was then used to remove the residual Ag nanoparticles for around 30 minutes.

A scanning electron microscope (SEM, Quanta FEG 250) was applied to characterize the morphology of the sample. The height of the Mie resonators was inspected by an atomic force microscopy (AFM, Agilent Technologies 5500 Scanning Probe Microscope). Reflectance of the quasi-random metasurface was measured by an angle-resolved microscope (ARM, angle-resolved spectrum system in micro-region, ideaoptics, China) equipped with a spectrometer with high sensitivity (NOVA, ideaoptics, China).

5. Results and discussion

5.1. Fabrication and morphology characterization

Figure 5(a) shows the SEM image of the Ag nanopattern after LIL. The energy of a single laser pulse was measured to be around 40 mJ, and the applied voltage of the laser source was around 560 V. The feature size of randomly distributed AgNHs gradually varies across the interference period or supercell from hundreds of nanometers to several tens of nanometers, while the pattern possesses periodic property in large scale. Figure 5(b) shows the corresponding quasi-random Mie-resonant metasurface A. The average height of the Mie resonators was inspected by an AFM to be around 400 nm (Figs. 5(c) and 5(d)). The Fourier transform of the metasurface A demonstrates the quasi-random property, which exists circular ring-shaped pattern (Fig. 5(e)).

5.2. Reflectance characterization and simulation

Broadband reflectance was corroborated by the measurement of reflectance spectra under normal incidence of surface A (Fig. 6(a)). Practically, perfect nanocylinder cannot be guaranteed, and the geometrical imperfections such as the random height, slanting sidewall and irregular surface are usually accompanied. However, these geometrical variations may be engineered to improve the broadband performance of the metasurface. Therefore, different metasurface designs (Fig. 6(c)) have been simulated by FDTD to compare their antireflection performance with the actual measured one.

The simulation region was chosen to be 0.8 μm by 9 μm with periodic boundary conditions in the X and Y directions due to the limited computing resources. For the metasurface composed of SiNPs with the variable radius, fixed height (400 nm) and random distribution (Fig. 2(c)), a relatively smooth reflectance spectrum was obtained, however, the overall reflectance was beyond 10%. Then, some Mie resonators, especially those with smaller radius at the bottom, were considered to be Si nanocones (SiNCs) with the fixed height (400 nm) and variable radius. The simulated overall reflectance of the metasurface composed of SiNP and SiNC was around 7.5%. In order to gain more insight into the geometry of the actual fabricated metasurface, the SEM images of the metasurface were obtained along a tilt angle. It was found that the Mie resonators could be modelled as truncated SiNCs as shown in Fig. 6(b3). Thus, a third metasurface composed of large SiNPs and small truncated SiNCs was simulated (Fig. 6(c)). The heights of the Mie resonators were fixed at 400 nm, and the top and bottom radii were variable. Furthermore, not only the radius variation and position randomness, but also the height variation (indicated by Fig. 6(b4)) of the Mie resonators should be considered, and therefore a fourth metasurface composed of large SiNPs and small truncated SiNCs with random heights was simulated (Fig. 6(a), 6(c)). The reflectance spectrum of the fourth metasurface agrees well

Optics EXPRESS

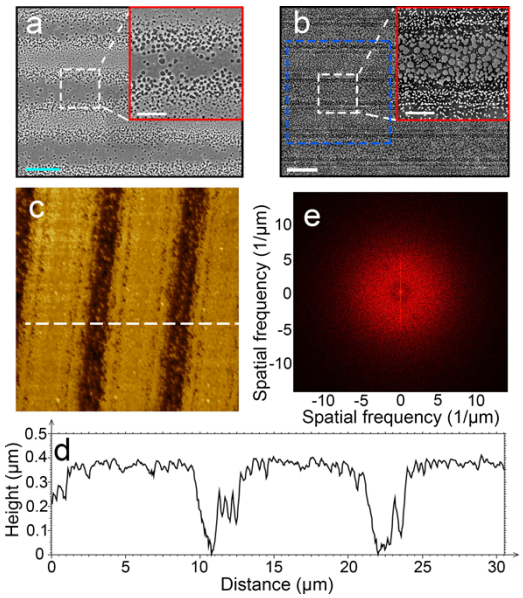

Fig. 5. Fabrication and characterization. (a) SEM photo of the quasi-random Ag pattern fabricated with a single laser pulse. (b) SEM photo of quasi-random metasurface A after MACE. The scale bars are 5 μm in (a, b), and 2.5 μm in the insets. (c) AFM image of metasurface A. (d) Height profile of the transversal section marked by the dashed line in (c). (e) Fourier transform of the SEM images of metasurfaces A, corresponding to Fig. 5(b) (marked by the blue dashed box).

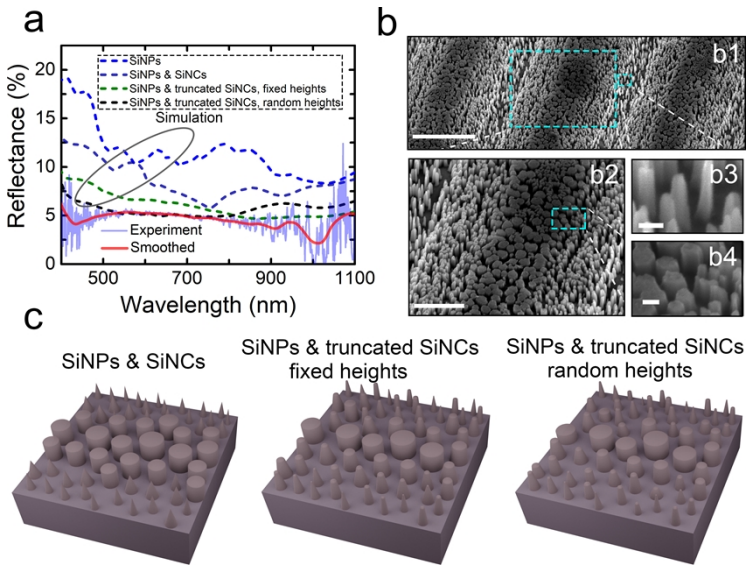

Fig. 6. (a) Simulated and measured reflection spectra of metasurface A. (b) SEM images (tilt view) of metasurface A. The scale bars are (b1) 5 μm, (b2) 2 μm, (b3) 200 nm, and (b4) 200 nm. (c) Simulated metasurface structures in Fig. 6(a).

Optics EXPRESS

with the measured spectrum, especially at the wavelength between 500 and 800 nm, and the reflectance value is almost fixed at 5%. Because the actual fabricated complex Mie resonators are simplified as truncated SiNCs with variable top/bottom radii and heights, there is a slight mismatch between the simulated and measured reflectance spectra.

5.3. Influence of top diameter and height variation of Mie resonators

In order to understand how the overall reflectance of the metasurface depends on the diameter and height variations of individual Mie resonators, we studied the Mie efficiency variation at respective situations. Figure 7(a) shows the Mie efficiency of truncated SiNCs on Si substrates with variable top diameters, and the bottom diameter and height were fixed at 200 nm and 400 nm, respectively. It was found that the resonances shifted with the increase of the top diameters. Therefore, more resonances contributing to broadband antireflection are introduced for a fixed bottom diameter, compared with that of SiNP and SiNC. That explains why the antireflection performance of the simulated third metasurface is better than that of the first and second metasurfaces. Moreover, the height variation of individual Mie resonators on Si substrates would also contribute to more resonances (Fig. 7(b)), where the top and bottom diameters of truncated SiNCs were fixed at 100 nm and 200 nm, respectively. Thus, the overall antireflection performance of the fourth metasurface outperforms the third one.

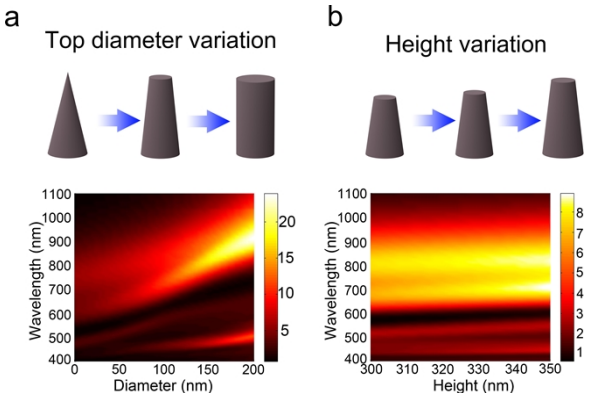

Fig. 7. Mie efficiency of Mie resonators with variable top diameters (a) and heights (b).

As discussed above, for the individual truncated SiNC with the fixed bottom diameter, the tuning of top diameter and height of the Mie resonator would contribute to spectral shift of resonances. In other words, abundant resonances covering a wide wavelength range can be achieved through the tuning of bottom diameter, top diameter and height of the truncated SiNCs. Most importantly, the resonances could overlap and merge together at a specific wavelength region for broadband applications. We focus on the broadband resonance enhancement. Therefore, multiple Mie resonators supporting different resonances would be favorable, and could be arranged quasi-randomly to form a metasurface that contributes to the efficient coupling among individual Mie resonators. This quasi-random property was realized by LIL, and could be controlled and tuned precisely by control over the LIL setup, such as the incident configuration, number of coherent beams, polarization and intensity.

5.4. Precise tuning of Mie-resonant metasurface

Figures 8(a) and 8(b) show two different metasurfaces fabricated by MACE of different AgNH patterns under different LIL conditions. The MACE condition is the same as that of the fabrication of metasurface A. Compared with metasurface A, individual Mie resonators in metasurfaces B and

Optics EXPRESS

C have different size distributions across one supercell, which may lead to different performances of antireflection depending on distinguishable scattering and diffraction. Figure 8(c) shows the measured reflectance curves of metasurfaces B and C. Metasurface B shows a near-uniform reflectivity of around 3% over the 400-1100 nm spectrum.

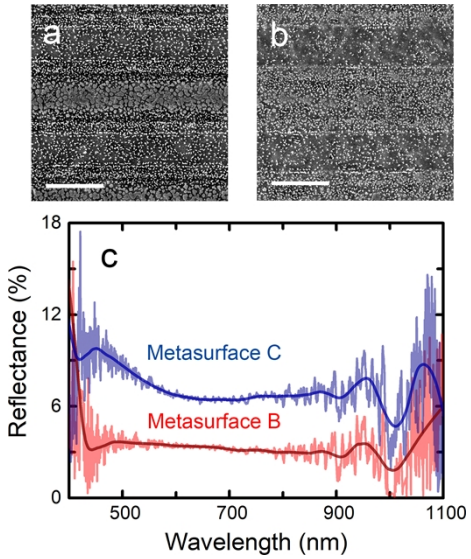

Fig. 8. Fabricated (a) metasurface B and (b) metasurface C with different size distributions. All scale bars are 5 µm. (c) Measured reflection spectra. The shaded areas represent the measured spectra, and the solid lines represent the smoothed spectra for each metasurface.

5.5. Scattering in momentum space

As the resonances provided by individual Mie resonators have different intensities and locations across the spectrum, when abundant of Mie resonators with different geometric shapes are engineered together to form the metasuface, the overall scattering responses as well as the reflectance spectra of metasurface depend on the different geometry of the Mie resonators.

Light scattering in a Mie-resonant photonic structure has multilevel and complex processes [43]. The first level involves Mie scattering by a single resonator. At the higher levels, for a photonic structure composed of identical resonators in an ordered system [44], such as photonic crystals [45] and quasicrystals [46–48], multiple Mie scattering by resonators interferes with each other, and results in Bragg scattering that contributes to the formation of photonic band gap. Here, we adopt the momentum space analysis to inspect the light scattering in the dielectric metasurface. In the momentum space, Bragg peaks are originated from the long-range order of the ordered system.

When disorder [49,50] or deformation is introduced in the ordered system [51], such as random positions or shape variations of the resonators, an additional scattering component including phase shift and amplitude fluctuations is added to the Bragg scattering, providing a broad background radiation and contributing to the formation of a continuum spectrum. This defect-induced continuum spectrum interferes with the relative narrow Bragg band, bringing about the Fano resonance [43,52], which tailors the strength of Anderson localization at a specific wavelength range.

Our proposed quasi-random Mie-resonant metasurface lies in the extremes between an ordered and disordered system. The corresponding Fourier spectra of the fabricated metasurfaces are

Optics EXPRESS

calculated and compared in the momentum space. Figures 5(e), 9(a) and 9(b) exhibit relatively flat and circular ring-shaped patterns, which corresponds to the formation of broad background. At the same time, a bright vertical line composed of Bragg peaks is manifested in each circumstance, which is resulted from the periodic two-beam interference pattern.

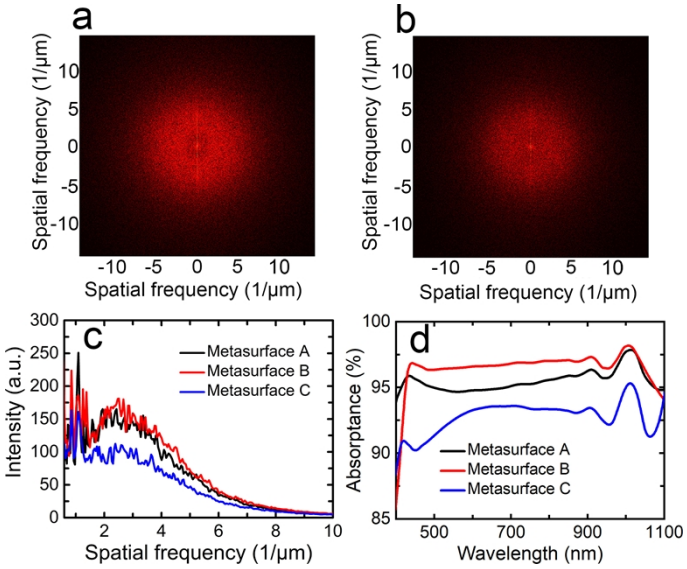

Fig. 9. Fourier transform of the SEM images of metasurfaces B (a) and C (b), corresponding to Fig. 8(a) and Fig. 8(b), respectively. (c) $PSD(f_r)$ curves for the three different metasurfaces. (d) Absorptance curves for the three different metasurfaces together with the substrate.

The overall scattering and diffraction responses of the metasurfaces can be revealed by their power spectral density (PSD) [53], which is defined by

$$PSD(f_x,f_y) = \frac{1}{L_xL_y}\left|\sum_{m=1}^{M}\sum_{n=1}^{N} f_{mn}e^{-i(f_xm\Delta L_x+f_yn\Delta L_y)}\Delta L_x\Delta L_y\right|^2 \tag{1}$$

where M and N are the maximum numbers of the pixels in the X and Y directions, L_x and L_y are the lengths of the SEM image in the X (horizontal) and Y (vertical) directions, f_{mn} is the pixel value at positions m and n, and $\Delta L_x = L_x/M$ and $\Delta L_y = L_y/N$ are the pixel sizes in the X and Y directions.

Because the discrete Fourier transform of the SEM image is defined by

$$F(f_x,f_y) = \Delta L_x\Delta L_y\sum_{m=1}^{M}\sum_{n=1}^{N} f_{mn}e^{-i(f_xm\Delta L_x+f_yn\Delta L_y)} \tag{2}$$

The following relationship can be obtained:

$$PSD(f_x,f_y) = \frac{1}{L_xL_y}|F(f_x,f_y)|^2 \tag{3}$$

Therefore, the distinct diffraction properties of different metasurfaces could be revealed by analyzing and comparing their Fourier transform. We focus on the radial spatial frequency f_r defined by $f_r^2 = f_x^2 + f_y^2$. Hence,

$$PSD(f_r) = \frac{1}{L_xL_y}|F(f_r)|^2 \tag{4}$$

The $PSD(f_r)$ distribution for the fabricated metasurfaces suggests a confined radial frequency range (Fig. 9(c)). The wavelength required for antireflection and light trapping covers from

Optics EXPRESS

400 nm to 1100 nm, and thus the spatial frequencies between 0.91 μm^{-1} and 2.5 μm^{-1} are required. The overall intensity of metasurface B is higher than that of metasurfaces A and C.

In order to find the relationship between the metasurface's antireflection property and $PSD(f_r)$. The absorptance values of corresponding metasurfaces together with the substrate (Fig. 9(d)) were obtained by $A = 1 - R$, where A is the absorptance and R is the reflectance, and the transmission can be neglected since the Si is 500 µm thick. The absorptance values (Fig. 9(d)) of the metasurfaces together with the substrate are confirmed by the spatial spectrum (Fig. 9(c)). The absorptance peaks at around 1000 nm (Fig. 9(d)) are revealed by the $PSD(f_r)$ peaks (Fig. 9(c)), which indicates the interference between periodicity-induced Bragg scattering and disorder-induced broadband and random Mie scattering, as shown by the bright vertical lines at the center of Fourier transform patterns (Figs. 5(e), 9(a) and 9(b)). Therefore, $PSD(f_r)$ can be used to efficiently compare and predict the antireflection properties of different metasurfaces.

The fabricated metasurfaces not only have broadband antireflection property, but also can achieve low reflectivity variations at large incident angles, which is important for solar cell application. Figure 10 shows the measured reflectance curves of metasurface B with different angles of incidences (AOIs). The overall reflectance can be around 5% with a large AOI of 40°.

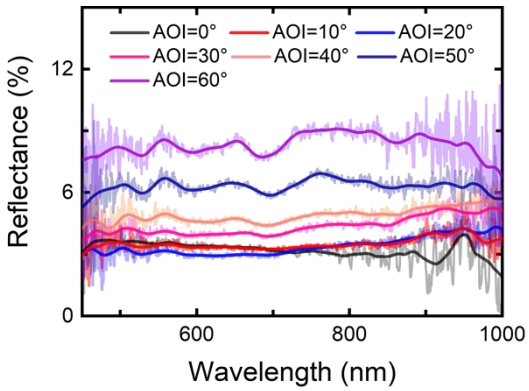

Fig. 10. Measured and the smoothed reflection spectra of metasurface B with different AOIs.

Metasurfaces with the lower broadband reflectivity could also be achieved by adjusting the LIL and MACE conditions. For example, the height, period and size distribution of a supercell can be effectively tuned. More complicated interference field distribution such as three-beam and six-beam interference (triangular and honeycomb lattices) will give more degree of freedom to fabricate complex quasi-random distributions of Mie resonators. Moreover, the wavelength region of interests aiming at uniform broadband reflection can be tuned by precisely adjusting the dewetting process of the metal films.

6. Conclusion

In conclusion, we take advantage of the quasi-random Mie resonators to achieve a novel ultrathin (around 400 nm) broadband antireflection coating. We have presented the LIIQP technique to fabricate quasi-random Mie-resonant metasurface in large scale. Our nanofabrication technique allows the efficient production of quasi-random metasurfaces with feature sizes down to one-tenth of the operating wavelength. Our proof-of-concept experiment suggests that the fabricated metasurface has a near-uniform reflectivity of around 3% over the 400-1100 nm spectral range without any complex coating process. Metasurfaces with lower broadband reflectivity or in a different spectrum region could be further achieved by optimizing the LIL and MACE conditions, i.e., height, period and size distribution of a supercell. More complicated interference field

Optics EXPRESS

distribution such as three-beam and six-beam interference will give more degree of freedom to fabricate complex quasi-random distributions of Mie resonators. To sum up, our concept and quasi-random nanofabrication methods provide a simple but efficient way to achieve antireflection over a broadband wavelength region of interests. Furthermore, the metasurface devices with random ordering could be used to study the disorder-induced light localization and energy harvesting.

Funding. National Key Research and Development Program of China (2016YFE0112100); EU H2020 Program (FabSurfWAR 644971, NanoStencil 767285); National Natural Science Foundation of China (11504030, N_HKU712/16); Jilin Provincial Science and Technology Program (20190201287JC, 20190702002GH, 20200901011SF, 2020C022-1); 111 Project (D17017); Research Grants Council of the Hong Kong Special Administrative Region of China (CityU T42-103/16-N, E-HKU701/17, HKU 17200219, HKU 17205321, HKU 17209018, HKU C7047-16G).

Acknowledgments. Publication made possible in part by support from the HKU Libraries Open Access Author Fund sponsored by the HKU Libraries.

Disclosures. The authors declare no conflicts of interest.

Data availability. Data underlying the results presented in this paper are not publicly available at this time but may be obtained from the authors upon reasonable request.

References

1. H. Chu, X. Xiong, Y.-J. Gao, J. Luo, H. Jing, C.-Y. Li, R. Peng, M. Wang, and Y. Lai, "Diffuse reflection and reciprocity-protected transmission via a random-flip metasurface," Sci. Adv. **7**(37), eabj0935 (2021).
2. S. I. Bae, Y. Lee, Y. H. Seo, and K. H. Jeong, "Antireflective structures on highly flexible and large area elastomer membrane for tunable liquid-filled endoscopic lens," Nanoscale **11**(3), 856–861 (2019).
3. G. Tan, J.-H. Lee, Y.-H. Lan, M.-K. Wei, L.-H. Peng, I. C. Cheng, and S.-T. Wu, "Broadband antireflection film with moth-eye-like structure for flexible display applications," Optica **4**(7), 678–683 (2017).
4. Y. Zhang, Y. Xu, S. Chen, H. Lu, K. Chen, Y. Cao, A. E. Miroshnichenko, M. Gu, and X. Li, "Ultra-Broadband Directional Scattering by Colloidally Lithographed High-Index Mie Resonant Oligomers and Their Energy-Harvesting Applications," ACS Appl. Mater. Interfaces **10**(19), 16776–16782 (2018).
5. S. F. Leung, Q. Zhang, M. M. Tavakoli, J. He, X. Mo, and Z. Fan, "Progress and Design Concerns of Nanostructured Solar Energy Harvesting Devices," Small **12**(19), 2536–2548 (2016).
6. J. Cai and L. Qi, "Recent advances in antireflective surfaces based on nanostructure arrays," Mater. Horiz. **2**(1), 37–53 (2015).
7. L. Zhao, Z. Wang, J. Zhang, L. Cao, L. Li, Y. Yue, and D. Li, "Antireflection silicon structures with hydrophobic property fabricated by three-beam laser interference," Appl. Surf. Sci. **346**, 574–579 (2015).
8. M. L. Brongersma, Y. Cui, and S. Fan, "Light management for photovoltaics using high-index nanostructures," Nat. Mater. **13**(5), 451–460 (2014).
9. J. Rombaut, S. Martínez, U. M. Matera, P. Mazumder, and V. Pruneri, "Antireflective Multilayer Surface with Self-Cleaning Subwavelength Structures," ACS Photonics **8**(3), 894–900 (2021).
10. C. F. Guo, T. Sun, F. Cao, Q. Liu, and Z. Ren, "Metallic nanostructures for light trapping in energy-harvesting devices," Light: Sci. Appl. **3**(4), e161 (2014).
11. M. Toma, G. Loget, and R. M. Corn, "Fabrication of broadband antireflective plasmonic gold nanocone arrays on flexible polymer films," Nano Lett. **13**(12), 6164–6169 (2013).
12. C. Wang, Z. Y. Jia, K. Zhang, Y. Zhou, R. H. Fan, X. Xiong, and R. W. Peng, "Broadband optical scattering in coupled silicon nanocylinders," J. Appl. Phys. **115**(24), 244312 (2014).
13. I. Staude, T. Pertsch, and Y. S. Kivshar, "All-Dielectric Resonant Meta-Optics Lightens up," ACS Photonics **6**(4), 802–814 (2019).
14. K. Koshelev and Y. Kivshar, "Dielectric Resonant Metaphotonics," ACS Photonics **8**(1), 102–112 (2021).
15. P. Spinelli, M. A. Verschuuren, and A. Polman, "Broadband omnidirectional antireflection coating based on subwavelength surface Mie resonators," Nat. Commun. **3**(1), 692 (2012).
16. S. Jahani and Z. Jacob, "All-dielectric metamaterials," Nat. Nanotechnol. **11**(1), 23–36 (2016).
17. S. Kruk and Y. Kivshar, "Functional Meta-Optics and Nanophotonics Governed by Mie Resonances," ACS Photonics **4**(11), 2638–2649 (2017).
18. Y. S. Guo, J. Zhou, C. W. Lan, H. Y. Wu, and K. Bi, "Mie-resonance-coupled total broadband transmission through a single subwavelength aperture," Appl. Phys. Lett. **104**(20), 204103 (2014).
19. Z. Weng and Y. Guo, "Broadband perfect optical absorption by coupled semiconductor resonator-based all-dielectric metasurface," Materials **12**(8), 1221 (2019).
20. T. Liu, R. Xu, P. Yu, Z. Wang, and J. Takahara, "Multipole and multimode engineering in Mie resonance-based metastructures," Nanophotonics **9**(5), 1115–1137 (2020).
21. A. Cordaro, J. van de Groep, S. Raza, E. F. Pecora, F. Priolo, and M. L. Brongersma, "Antireflection High-Index Metasurfaces Combining Mie and Fabry-Pérot Resonances," ACS Photonics **6**(2), 453–459 (2019).

Optics EXPRESS

22. E. F. Pecora, A. Cordaro, P. G. Kik, and M. L. Brongersma, "Broadband Antireflection Coatings Employing Multiresonant Dielectric Metasurfaces," ACS Photonics **5**(11), 4456–4462 (2018).
23. E. R. Martins, J. Li, Y. Liu, J. Zhou, and T. F. Krauss, "Engineering gratings for light trapping in photovoltaics: The supercell concept," Phys. Rev. B **86**(4), 041404 (2012).
24. W. K. Lee, S. Yu, C. J. Engel, T. Reese, D. Rhee, W. Chen, and T. W. Odom, "Concurrent design of quasi-random photonic nanostructures," Proc. Natl. Acad. Sci. U.S.A. **114**(33), 8734–8739 (2017).
25. E. R. Martins, J. Li, Y. Liu, V. Depauw, Z. Chen, J. Zhou, and T. F. Krauss, "Deterministic quasi-random nanostructures for photon control," Nat. Commun. **4**(1), 2665 (2013).
26. A. J. Smith, C. Wang, D. Guo, C. Sun, and J. Huang, "Repurposing Blu-ray movie discs as quasi-random nanoimprinting templates for photon management," Nat. Commun. **5**(1), 5517 (2014).
27. M. Segev, Y. Silberberg, and D. N. Christodoulides, "Anderson localization of light," Nat. Photonics **7**(3), 197–204 (2013).
28. T. Crane, O. J. Trojak, J. P. Vasco, S. Hughes, and L. Sapienza, "Anderson Localization of Visible Light on a Nanophotonic Chip," ACS Photonics **4**(9), 2274–2280 (2017).
29. T. Schwartz, G. Bartal, S. Fishman, and M. Segev, "Transport and Anderson localization in disordered two-dimensional photonic lattices," Nature **446**(7131), 52–55 (2007).
30. B. Lechthaler, T. Fox, S. Slawik, and F. Mücklich, "Direct laser interference patterning combined with mask imaging," Opt. Laser Technol. **123**, 105918 (2020).
31. J. van de Groep and A. Polman, "Designing dielectric resonators on substrates: combining magnetic and electric resonances," Opt. Express **21**(22), 26285–26302 (2013).
32. E. D. Palik, *Handbook of Optical Constants of Solids* (Academic, New York, 1985).
33. U. Zywietz, M. K. Schmidt, A. B. Evlyukhin, C. Reinhardt, J. Aizpurua, and B. N. Chichkov, "Electromagnetic Resonances of Silicon Nanoparticle Dimers in the Visible," ACS Photonics **2**(7), 913–920 (2015).
34. J. van de Groep, T. Coenen, S. A. Mann, and A. Polman, "Direct imaging of hybridized eigenmodes in coupled silicon nanoparticles," Optica **3**(1), 93–99 (2016).
35. A. Mirzaei and A. E. Miroshnichenko, "Electric and magnetic hotspots in dielectric nanowire dimers," Nanoscale **7**(14), 5963–5968 (2015).
36. K. Bi, D. Yang, J. Chen, Q. Wang, H. Wu, C. Lan, and Y. Yang, "Experimental demonstration of ultra-large-scale terahertz all-dielectric metamaterials," Photonics Res. **7**(4), 457–463 (2019).
37. P. Xie, Z. Wang, Z. Zhang, R. Fan, C. Cheng, H. Liu, Y. Liu, T. Li, C. Yan, N. Wang, and Z. Guo, "Silica microsphere templated self-assembly of a three-dimensional carbon network with stable radio-frequency negative permittivity and low dielectric loss," J. Mater. Chem. C **6**(19), 5239–5249 (2018).
38. K. Bi, Q. Wang, J. Xu, L. Chen, C. Lan, and M. Lei, "All-dielectric metamaterial fabrication techniques," Adv. Opt. Mater. **9**(1), 2001474 (2021).
39. C. Huo, J. Wang, H. Fu, X. Li, Y. Yang, H. Wang, A. Mateen, G. Farid, and K.-Q. Peng, "Metal-assisted chemical etching of silicon in oxidizing HF solutions: origin, mechanism, development, and black silicon solar cell application," Adv. Funct. Mater. **30**(52), 2005744 (2020).
40. X. Guo, L. Li, Y. Hu, L. Cao, L. Dong, L. Wang, R. Ding, Z. Weng, Z. Song, H. Xu, Z. Yang, X. Liu, Y. Tian, and Z. Wang, "Superlens-enhanced laser interference lithography," Appl. Phys. Express **11**(12), 125201 (2018).
41. X. Guo, S. Li, Z. Lei, R. Liu, L. Li, L. Wang, L. Dong, K. Peng, and Z. Wang, "Controllable Patterning of Hybrid Silicon Nanowire and Nanohole Arrays by Laser Interference Lithography," Phys. Status Solidi RRL **14**(6), 2000024 (2020).
42. J. Berzins, S. Indrisiunas, K. van Erve, A. Nagarajan, S. Fasold, M. Steinert, G. Gerini, P. Gecys, T. Pertsch, S. M. B. Baumer, and F. Setzpfandt, "Direct and High-Throughput Fabrication of Mie-Resonant Metasurfaces via Single-Pulse Laser Interference," ACS Nano **14**(5), 6138–6149 (2020).
43. M. V. Rybin, A. B. Khanikaev, M. Inoue, K. B. Samusev, M. J. Steel, G. Yushin, and M. F. Limonov, "Fano resonance between Mie and Bragg scattering in photonic crystals," Phys. Rev. Lett. **103**(2), 023901 (2009).
44. S. Yu, C.-W. Qiu, Y. Chong, S. Torquato, and N. Park, "Engineered disorder in photonics," Nat. Rev. Mater. **6**(3), 226–243 (2020).
45. C. Pouya, D. G. Stavenga, and P. Vukusic, "Discovery of ordered and quasi-ordered photonic crystal structures in the scales of the beetle Eupholus magnificus," Opt. Express **19**(12), 11355–11364 (2011).
46. M. Florescu, S. Torquato, and P. J. Steinhardt, "Complete band gaps in two-dimensional photonic quasicrystals," Phys. Rev. B **80**(15), 155112 (2009).
47. K. Viebahn, M. Sbroscia, E. Carter, J. C. Yu, and U. Schneider, "Matter-Wave Diffraction from a Quasicrystalline Optical Lattice," Phys. Rev. Lett. **122**(11), 110404 (2019).
48. Z. Che, Y. Zhang, W. Liu, M. Zhao, J. Wang, W. Zhang, F. Guan, X. Liu, W. Liu, L. Shi, and J. Zi, "Polarization Singularities of Photonic Quasicrystals in Momentum Space," Phys. Rev. Lett. **127**(4), 043901 (2021).
49. S. Yu, X. Piao, J. Hong, and N. Park, "Metadisorder for designer light in random systems," Sci. Adv. **2**(10), e1501851 (2016).
50. E. Maguid, M. Yannai, A. Faerman, I. Yulevich, V. Kleiner, and E. Hasman, "Disorder-induced optical transition from spin Hall to random Rashba effect," Science **358**(6369), 1411–1415 (2017).
51. Z. Xu, X. Kong, R. J. Davis, D. a. Bisharat, Y. Zhou, X. Yin, and D. F. Sievenpiper, "Topological valley transport under long-range deformations," Phys. Rev. Res. **2**(1), 013209 (2020).

Optics EXPRESS

52. A. N. Poddubny, M. V. Rybin, M. F. Limonov, and Y. S. Kivshar, "Fano interference governs wave transport in disordered systems," Nat. Commun. **3**(1), 914 (2012).
53. M. C. van Lare and A. Polman, "Optimized Scattering Power Spectral Density of Photovoltaic Light-Trapping Patterns," ACS Photonics **2**(7), 822–831 (2015).